V International Conference on Simulation for Additive Manufacturing
Sim-AM 2025
F. Auricchio, M. Carraturo and S. Morganti (Eds)

VARIATIONS IN MORPHOLOGY AND MICROSTRUCTURE CAUSED BY DIFFERENT MELT POOL DYNAMICS IN PBF-L

MARIA BOGDANOVA[1], ANASTASIA PEREPELKINA[2,3], ANDREY ZAKIROV[2], SERGEI BELOUSOV[1], BORIS KORNEEV[1], INNA ISKANDAROVA[2] AND BORIS POTAPKIN[2]

[1]Hipercone Ltd., 9434314, 14 Ezrat Israel St., Jerusalem, Israel e-mail: belousov@hipercone.com, web page: https://www.hipercone.com/
[2] Kintech Lab Ltd., 123298, 3rd Khoroshevskaya St. 12, Moscow, Russia
[3] Keldysh Institute of Applied Mathematics, 125047, Miusskaya sq., 4, Moscow, Russia

Key words: numerical simulations, PBF-L, meltpool shape, thin wall, grain growth

Abstract. A multi-layer mesoscale numerical study of microstructure evolution and morphology formation in thin walls fabricated by laser powder bed fusion of Inconel 625 is presented. Simulations were performed using the KiSSAM code, which couples powder spreading via discrete element modeling, melt pool hydrodynamics with a free surface lattice Boltzmann method, and grain growth using cellular automata. The effect of laser scanning strategies and processing regimes on grain morphology was investigated. The results show that while zigzag scanning improves wall uniformity and reduces lack-of-fusion defects, the grain structure is predominantly governed by laser power and scanning speed. Increased scanning speed leads to unstable melt pool and non-uniform temperature gradients, disrupting epitaxial grain growth and promoting grain misorientation.

1 INTRODUCTION

Various studies have explored the limits of thin wall fabrication with laser powder bed fusion (PBF-L) [1–3]. For a particular thickness of about 200 microns or less, building a high-quality thin wall becomes a challenging problem due to the lack of fusion, porosity defects [3], and distortion [4]. Extensive research has examined the link between build quality and microstructural evolution [5, 6]. A key research direction is to establish how processing parameters dictate the transition between epitaxial and equiaxed grains, and how this transition is governed by heat and mass transfer [7,8]. The objective of the present study is to elucidate the role of melt pool dynamics, as well as the influence of scanning strategy and processing parameters, on the morphology and microstructural characteristics of thin-wall structures.

To improve understanding of the multiphysical processes that take place during the PBF-L process, a numerical simulation is actively applied [9–11]. Current research is focused on a melt pool (mesoscopic) scale of the process [12]. For mesoscale simulation, we have developed and used the simulation software for additive manufacturing KiSSAM [13–17]. In our previous work [18], it was shown that the correct description of the free surface of the melting pool and the wetting behavior is a key factor for the accurate prediction of the morphology of thin wall parts, allowing an accurate prediction of the wall morphology [19–21]. In these works, the melt pool simulation is coupled with the grain structure simulation, allowing us to capture the effect of the melt pool dynamics on grain growth.

Related works [22,23] used the DEM-CFD-CA approach to simulate the PBF process in nickel superalloys, where the discrete element method (DEM) is used for the simulation of powder spreading, the computational fluid dynamics (CFD) is used for the melt pool modeling, and the cellular automata (CA) method is used for grain structure calculation. The study on Inconel 718 [22] examines the multilayer, multitrack evolution of the grain structure, emphasizing how the hatch distance influences the grain morphology. Numerical results show that larger hatch distances produce more equiaxed grains with reduced grain anisotropy. The study on Inconel 625 [23] focuses on analyzing melt pool evolution, temperature fields, defect formation, and grain nucleation under varying laser energy densities. An optimal energy range is identified to minimize defects and promote controlled epitaxial growth. Both papers use a simplified laser absorption model without taking into account multiple reflections of the laser beam. The effect of powder wetting by the melt was also omitted, as the ideal wetting is assumed between the melt and the powder, which is known to be very important [18] for thin-wall structures. There are a limited number of simulation studies with thin wall investigation from the point of view of grains formation throughout the layers [24] as it requires simulation of dozens of layers which is computationally exhausting.

In the current research, walls that have the thickness of a single track are considered, which some researchers refer to as ultrathin walls [25, 26]. In most of the studies to the authors' knowledge, ultrathin or single-track thin walls have been fabricated using the unidirectional scanning strategy in which all layers have been deposited in the same direction [8, 25–28]. However, unidirectional scanning is not the only viable strategy for thin-wall fabrication. In [29], bidirectional scanning was used, however, the result was not compared to the unidirectional scan.

Here we compare two scanning strategies: 1) unidirectional scanning (all layers built in the same direction) and 2) zigzag scanning (alternating scanning direction between layers). For the selected strategy, we vary the laser power and scanning speed to analyze the effect of different melting regimes on both wall morphology and microstructure. By comparing the numerical results for walls fabricated under different conditions, we aim to derive key insights into how processing parameters influence final morphology and grain structure. The size and orientation of the grains affect the strength, stiffness, and creep resistance [30, 31] and the modeled grain distributions and statistical characteristics can be further used to predict mechanical performance and guide process optimization.

2 METHODS

2.1 Free Surface Lattice Boltzmann Method

For simulation of the additive manufacturing process, we use KiSSAM software [13, 14, 16]. It includes models for the three crucial phenomena of additive manufacturing at the mesoscale: powder spreading, multiphase meltpool dynamics, and heat transfer. The fluid dynamics of the meltpool is simulated with the free surface thermal lattice Boltzmann method (LBM) [32]. The lattice Boltzmann method [33] solves fluid dynamics equations on a uniform Cartesian mesh. The fluid surface is tracked with the volume of fluid approach [34].

The mesh is dynamic and is updated during the simulation to contain only the area around the fluid metal. Heat transfer is modeled with LBM using the double discrete function approach in the melt area, and on a separate mesh around it. This allows us to maintain high resolution for the 3D fluid surface and to track temperature in an area of up to a few cubic centimeters at the same time. With the use of sparse voxels storage the morphology of a printed part is available in high resolution in an area of several cubic millimeters (the detailed description of the model can be found in [13, 14]).

Ray tracing with account for multiple reflections and energy absorption is used to simulate the

energy source. The surface curvature is found with the template sphere approach [32], and surface wetting is taken into account. Marangoni convection and surface pressure are modeled on the surface, as well as the radiation cooling and the drag force in the mushy zone. Evaporation is taken into account by estimating the energy and mass loss and the recoil pressure with the evaporation solver.

To simulate the dynamics of the powder particles during spreading, the PowDEM utility is used [13]. It is developed on the basis of an open-source DEM code Blaze-DEMGPU [35], which was significantly adapted and improved for AM powder bed simulations [14, 18].

2.2 Grains Growth Model

We use the cellular automata (CA) approach to simulate the process of grain formation, growth, development and change during the melt pool solidification and remelting. We chose the CA model based on the method by Gandin and Rappaz [36]. CA models are becoming mainstream for microstructure modeling in metallic materials [37]. They were successfully combined with other numerical methods [38, 39], and used to simulate grain structure in additive manufacturing [40, 41]. Here, we implement the algorithm as described in [42].

A grain is represented as an octahedron coincident with the $<100>$ grain orientation. The orientation of each octahedron is described by Euler angles. Each non-liquid mesh cell is assigned an octahedron with corresponding directions.

The phase transition is modeled as follows. Each cell can be in one of the three states: liquid, solid, and interface. If the temperature is higher than the liquidus temperature, the cell state changes to liquid. The state of other cells changes so that no liquid cell is adjacent to a solid cell: the cells between solid and liquid change to the interface state. Each interface cell is assigned an octahedron orientation, as well as the octahedron size l (half of the diagonal). This octahedron size growth rate depends only on the local temperature T according to $v(\Delta T) = \eta_1 \Delta T + \eta_2 \Delta T^2 + \eta_3 \Delta T^3$, where $\Delta T = \max(T_{liquidus} - T, 0)$ is the local undercooling, and η_1, η_2, η_3 are the fitting coefficients for a chosen material.

When the octahedron for a given cell C_α becomes large enough to consume the center of the neighboring cell C_β, the C_β cell is considered to be captured by the C_α cell. Thus, in C_β, the new octahedron is initialized with the corresponding size and position. The new octahedron direction is inherited from the octahedron direction of the cell C_α.

2.3 Multilayer Part Manufacturing

The simulation of a part manufacturing is a multistage process. In the KiSSAM simulation procedure, in the very beginning, powder deposition on a plain substrate is simulated. After the powder simulation is finalized, the main part of the simulation is performed. The powder is melted with the energy source, and the motion of the fluid, its solidification, heat transfer, and grain growth are modeled simultaneously. After the scanning is finished and all material is solidified, the volumetric data of the solid fraction on the mesh are cleaned up and converted to surface data. Powder deposition on the new surface is simulated. The process is repeated in order to obtain the desired number of layers in the simulation. Information about the grain structure persists between the layers.

3 PARAMETERS AND VALIDATION

The material properties of the Inconel 625 alloy (Table 1) were validated in our previous studies, where we established that our model reproduces the depth and width of the track, as well as the melting regime (balling, keyholing) with sufficient accuracy [43], and reproduced the morphology of

Table 1: Thermophysical properties of the Inconel 625 alloy. T is the temperature in K

Density at $T_{liquidus}$, kg/m^3	8000
Viscosity, m^2/s	$0.7 \cdot 10^{-6}$
Liquidus temperature, K	1623
Solidus temperature, K	1563
Surface tension, N/m	$2.4470 - 3.5000 \cdot 10^{-4}T$
Wetting angle with substrate surface, °	10
Wetting angle with powder particles, °	105
Diffusivity at solid phase, m^2/s	$2.31400 \cdot 10^{-6} + 2.0000 \cdot 10^{-9}T$
Diffusivity at liquid phase, m^2/s	$2.43400 \cdot 10^{-6} + 2.0000 \cdot 10^{-9}T$
Isobaric volumetric heat capacity, J/m^3/K	$\begin{cases} 4.00 \cdot 10^6, & \text{if } 0 < T \leq 900K \\ 5.50 \cdot 10^6, & \text{if } 900K < T \leq 1563K \\ 6.00 \cdot 10^6, & \text{if } T > 1563K \end{cases}$
Absorption coefficient for solid/liquid phase	0.3
Latent heat of melting, J/m^3	$2.656 \cdot 10^9$
Saturated vapour pressure (Antoine model)	$P_{sat}(T) = 10^{\mathcal{A}-\mathcal{B}/(\mathcal{C}+T)}$ Pa $\mathcal{A} = 11.672, \mathcal{B} = 20765.0, \mathcal{C} = 0$

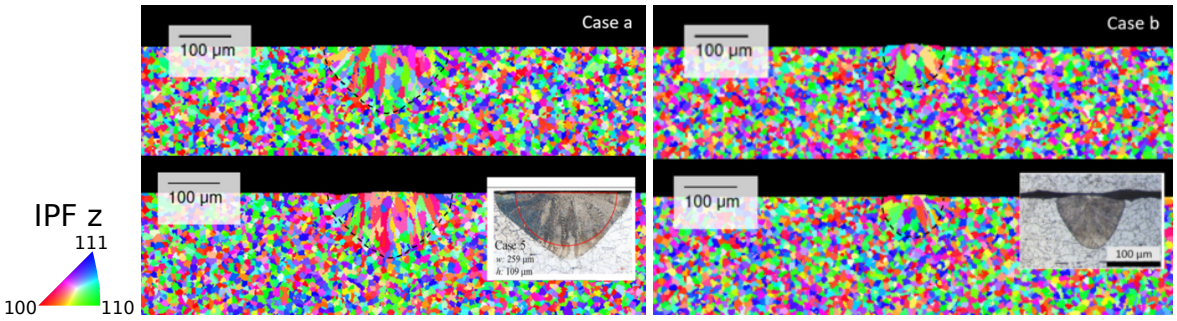

Figure 1: Transversal cross-sections of grains microstructure for single tracks. Experimental results are taken from [45] (left sub-figure) and [46] (right sub-figure). The remelted area is indicated with a black dash line. Upper figures are obtained with the mesh step of 3 µm and lower figures – with the mesh step of 2 µm.

thin walls in PBF-L [18].

To initialize the grain growth model, we set an initial distribution of the grains and their orientation in the substrate and in the powder. The size of the grains in the substrate was chosen in agreement with the experiments published in [44]. The size of a single grain is $10 \div 20$ µm. The orientation of grains in the powder particles were generated at random and each particle contains a single grain.

For the grain growth rate we used the values reported in [42]: $\eta_1 = 1.77 \cdot 10^{-5}\text{m}/(\text{s} \cdot \text{K})$, $\eta_2 = 1.58 \cdot 10^{-5}\text{m}/(\text{s} \cdot \text{K}^2)$, $\eta_3 = 2.29 \cdot 10^{-6}\text{m}/(\text{s} \cdot \text{K}^3)$. For bulk nucleation we used the heterogeneous model with Gaussian distribution, where the density of grains depends on the degree of undercooling (ΔT) with the maximal undercooling temperature $T_{max} = 9.5K$ and the standard deviation $\sigma = 2K$. The average density of bulk nuclei was 10^{14}m^{-3}.

To validate the performance of the model and the microstructure growth parameters for Inconel 625, we selected several studies that present experimentally obtained cross-sections of single tracks on a substrate with a well-defined grain structure [45, 46].

We have modeled the two cases, in which the laser speed, power and spot size parameters were

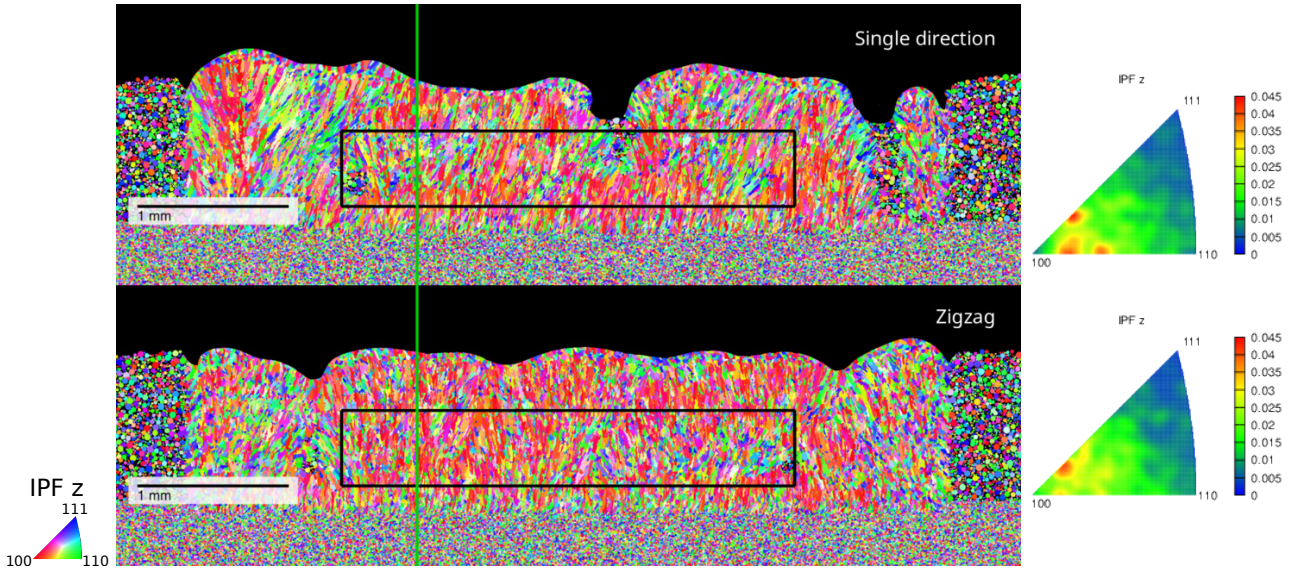

Figure 2: Microstructure in the central longitudinal section of the two walls (24 layers) printed with two different strategies: cases S-V600-P195 (top), and Z-V600-P195 (bottom). The green line is the position of the cross-section in Fig. 3. The IPF figures are made with the statistics collected in the black box.

$V = 200$ mm/s, $P = 195$ W, $D_{4\sigma} = 170$ µm (case a), and $V = 800$ mm/s, $P = 195$ W, $D_{4\sigma} = 100$ µm (case b) correspondingly (Fig. 1). The grains in the remelted zone grow inward, originating from the grains of the substrate. The growth direction is close to the normal to the boundary of the melt pool. The grain thickness is $10 \div 20$ µm and the length is approximately half the width of the track, which is in agreement with the experiment. We performed this experiment with 2 µm, 3 µm and 4 µm mesh steps, and observed that the grid resolution of 3 µm is sufficient to see the relevant fine grains; therefore, in further experiments, we use this value in both the fluid dynamic model and the CA model.

Table 2: The summary of the simulations reported in Section 4.

Case ID	Strategy	V, mm/s	P, W	layers
S-V600-P195	Single direction	600	195	24
S-V1058-P349	Single direction	1058	349	24
Z-V600-P195	Zig-zag	600	195	14, 24
Z-V1058-P349	Zig-zag	1058	349	14
Z-V1600-P500	Zig-zag	1600	500	14

4 RESULTS

We performed a series of numerical simulations in which a wall was constructed with the width of a single laser pass and a length of 5 mm. Both the scanning strategy and the laser operating parameters were varied (Table 2) The S-V1058-P349 case corresponds to the parameters used in [18, 47]. The motivation for the parameters chosen in the other cases is explained in the following sections.

The simulation volume is $6 \times 1 \times 3$ mm^3, and the flat substrate is initially in the $0 < z < 1$ mm area. The laser moves from $x, y = (0.5, 0.5)$ mm to $x, y = (5.5, 0.5)$ mm (and back, if zigzag scanning is applied). The platform step is 40 µm. The powder is assumed to be spherical with particle sizes between $15 \div 45$ µm. One layer scan simulation took $5 \div 13$ hours of wall time.

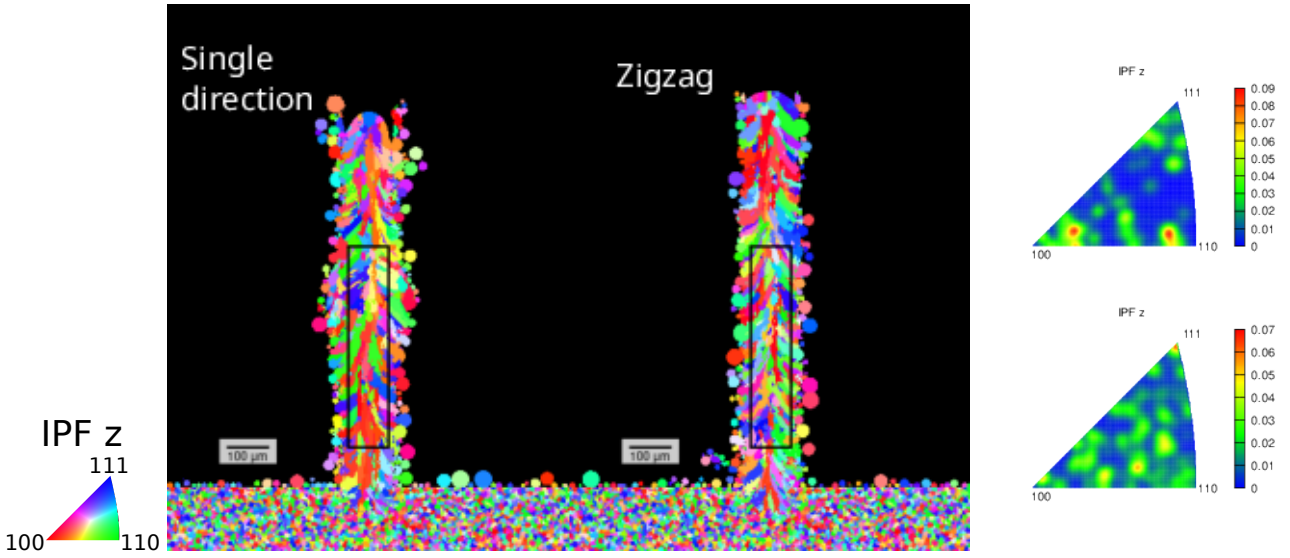

Figure 3: Microstructure in the transversal cross-section (1.5 mm from the scan path starting point) of the two walls (24 layers). The powder particles which did not touch the melt pool during the simulation are removed in the visualization. The IPF figures are made with the statistics collected in the black box.

First, we compare S-V600-P195 (single-direction) and Z-V600-P195 (zigzag snake pattern) cases to investigate the influence of scanning strategy on wall morphology and microstructure (Fig. 2).

Both walls have a lack of fusion regions, which can be caused by the disintegration of the melt pool into separate droplets during the melting of a certain layer. The height of the wall is more homogeneous for the zigzag strategy. In the transverse cross-section of the wall (Fig. 3), we see that the grains grow predominantly along the building direction, deviating slightly from the vertical in a random manner. This behavior is expected because the grains are likely to grow in the normal direction to the solidification front.

Table 3: Melt pool characteristics averaged over the relatively stable part of each track.

	600 mm/s, 195 W	1058 mm/s, 349 W	1600 mm/s, 500 W
Melt pool depth, μm	71	105	86
Melt pool width, μm	116	120	118
Melt pool length, mm	0.84	1.7	2.0

Based on the results of studies [48,49], we initially expected to observe changes in the grain growth pattern when switching from a unidirectional to a bidirectional scanning strategy. Specifically, we anticipated that, in the longitudinal section, vertical grains would grow at different angles in adjacent layers, forming a wavy structure. However, as shown in Fig. 2, no such change in grain growth behavior is observed. This can be explained by the fact that when a layer is deposited with a width of a single laser pass, the melt pool tends to accumulate into droplets and becomes discontinuous. As a result, the characteristic tilt of the grains in each subsequent layer is not visible.

In the further, we focus on the zig-zag strategy and analyze how the laser operating parameters influence both the morphology and the microstructure.

Knowing that grain growth is normal to the solidification front, we expect that the shape of the melt pool affects grain growth. To exclude other factors, we chose regimes in which the melt depth is similar but the melt length is different. To find the regimes best suited for the study, we performed

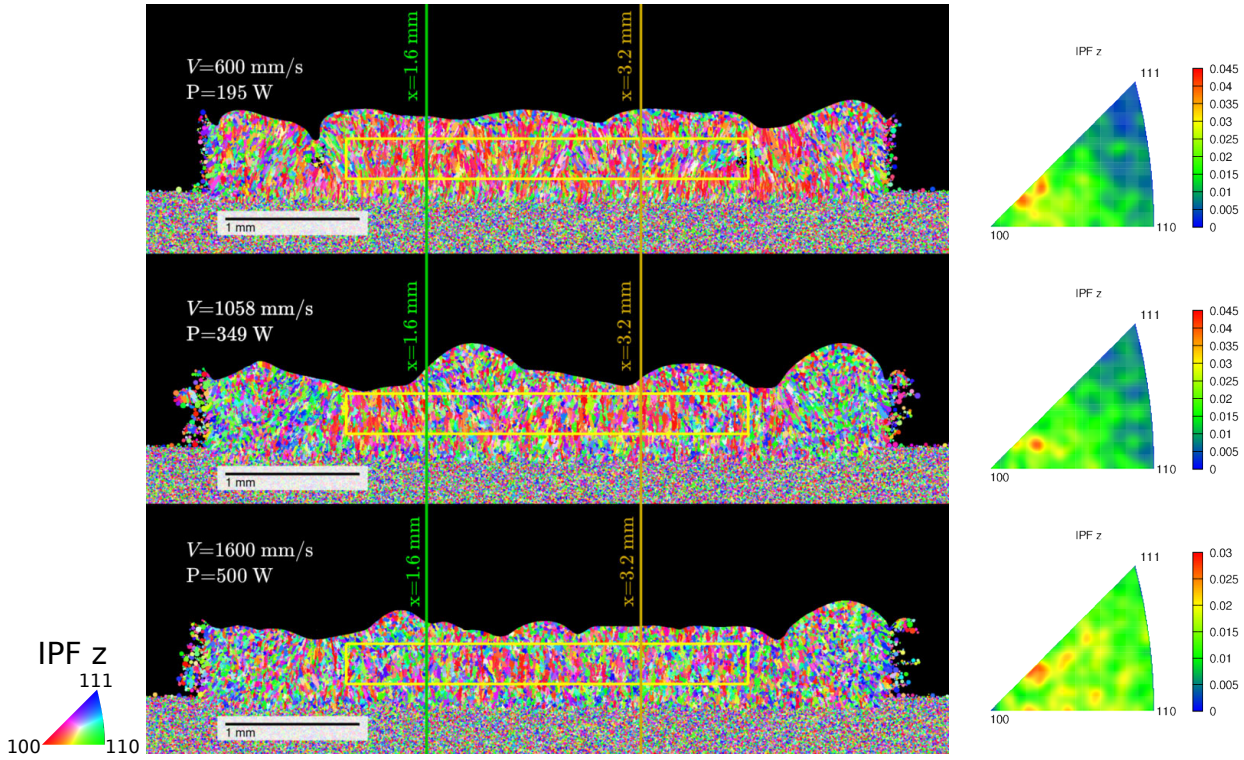

Figure 4: Longitudinal cross-section of the grain microstructure for three walls (14 layers). The colored lines indicate the position of cross-sections in Fig. 5. The IPF figures are made with the statistics collected in the yellow box.

preliminary calculations of a process map for single tracks on a powder layer and determined the dependence of the melt pool depth and length on laser speed and power, with a beam size of $D_{4\sigma} = 100$ µm. The laser speed and power were varied within a range corresponding to the operational parameters for the Inconel 625 alloy [47].

After this study, we selected the two regimes in which the melt depth was approximately 80 µm (close to one obtained with the baseline parameters in S-V1058-P349 case), but the scanning speed, and, consequently, the melt pool length, differed significantly (Table 3).

With lower speeds, the melt pool is more stable and the number of droplets is smaller. As the speed increases, the melt pool becomes less stable, splashes appear, and individual droplets fly away from the track and settle on the powder layer. This unstable behavior of the melt pool is expected to result in irregularity in the wall shape after several layers are deposited.

The length of the melt pool increases with increasing speed. Its bottom becomes more horizontal, and the direction of the temperature gradient changes. We expect that it may influence the grain growth.

In the further, we compare cases Z-V600-P195, Z-V1058-P349, and Z-V1600-P500 (Table 2).

In the central cross-section (Fig. 4), a more uniform shape is observed at a higher scanning speed. On the other hand, an increase in scanning speed leads to the ejection of numerous droplets from the melt pool, with droplet sizes comparable to wall thickness. These droplets settle onto the powder layer near the wall and fuse to it. As a result, the lateral surface of the wall at high scanning speed is more rough and its width is less uniform.

In the longitudinal cross-sections (Fig. 4), we observe that in case of low velocity, the long grains grow throughout several layers with crystallographic orientation mainly along the <100> direction. For high velocity, significantly less <100> grains are observed. Note that this effect is due to the

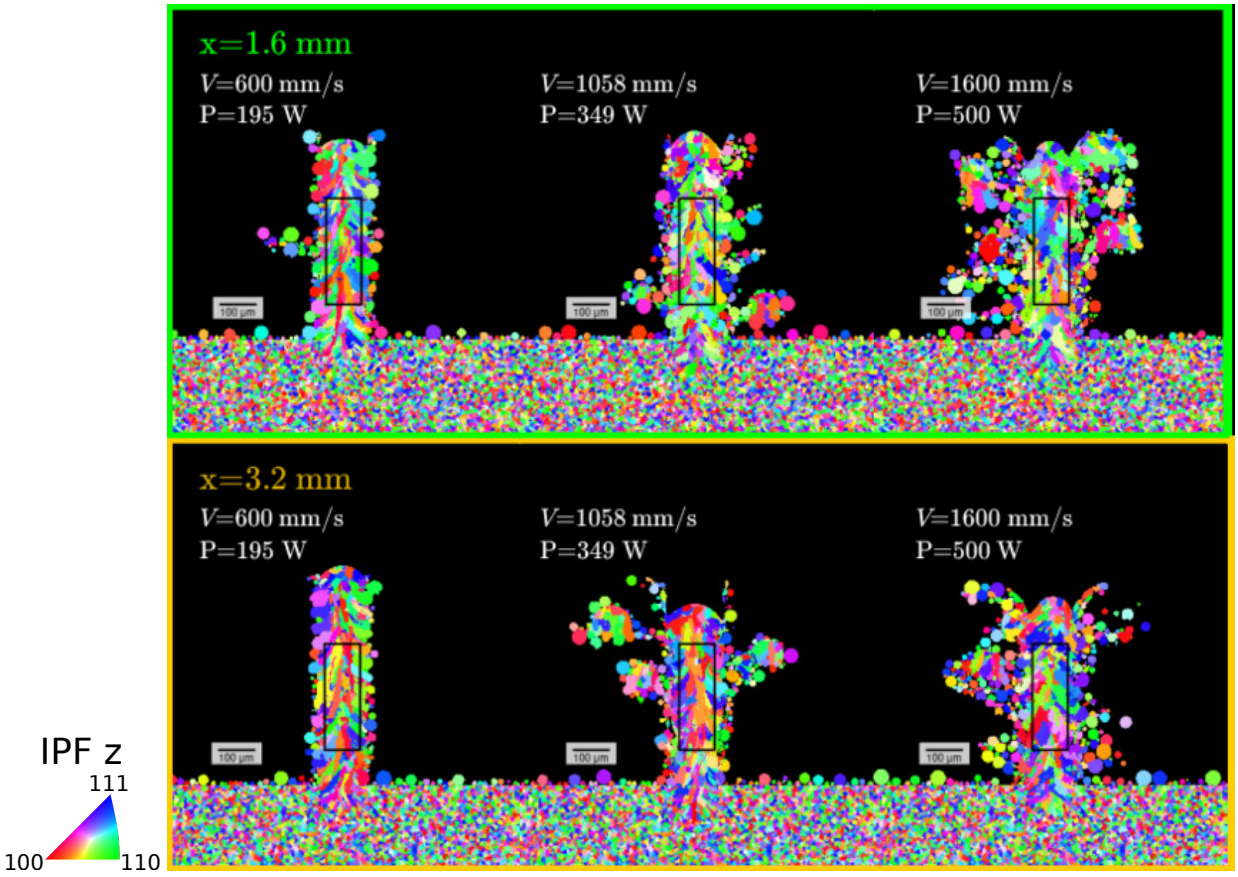

Figure 5: Transversal cross-sections of three walls. The IPF figures (Fig. 6) are made with the statistics collected in the black box.

difference in scanning speed but not in the scanning direction. It can be seen in Fig. 2, where the microstructure of two walls with the same laser velocity, but different strategies, is shown: the long <100> grains are dominant in both cases.

The IPF maps (Fig. 5) and the corresponding IPFs (Fig. 6) built using the transverse cross-sections do not show any pronounced grain orientation compared to those built at the longitudinal cross-sections (Fig. 4). This can be explained by the fact that the grains along the edges of the wall cross-section are mainly the ones that grow from the powder particles and therefore they have random orientation, which allows the germination of grains through several layers of the wall to play a dominant role only in a narrow central section of the wall.

The grains are known to grow epitaxially, predominantly in the direction of the temperature gradient, which is perpendicular to the moving solidification front [6, 48]. For grains to grow vertically through multiple layers, the melt pool must have a flat bottom, and its shape must remain stable along the single track. After several layers have been built, the primary heat dissipation during melt pool cooling is directed downward into the solidified region, because the thermal conductivity of the powder is significantly lower than that of the bulk material. However, when droplets and other irregularities form in the melt pool, random thickened areas may appear around the wall. In such places, where the wall becomes thicker, the shape of the melt pool (including its bottom) is distorted and no longer remains flat. The melt pool can also become asymmetric in relation to the center of the wall. Such distortions in geometry lead to changes in the direction of the temperature gradient, which prevent grains from growing strictly upward. This effect is precisely what we observe in the wall

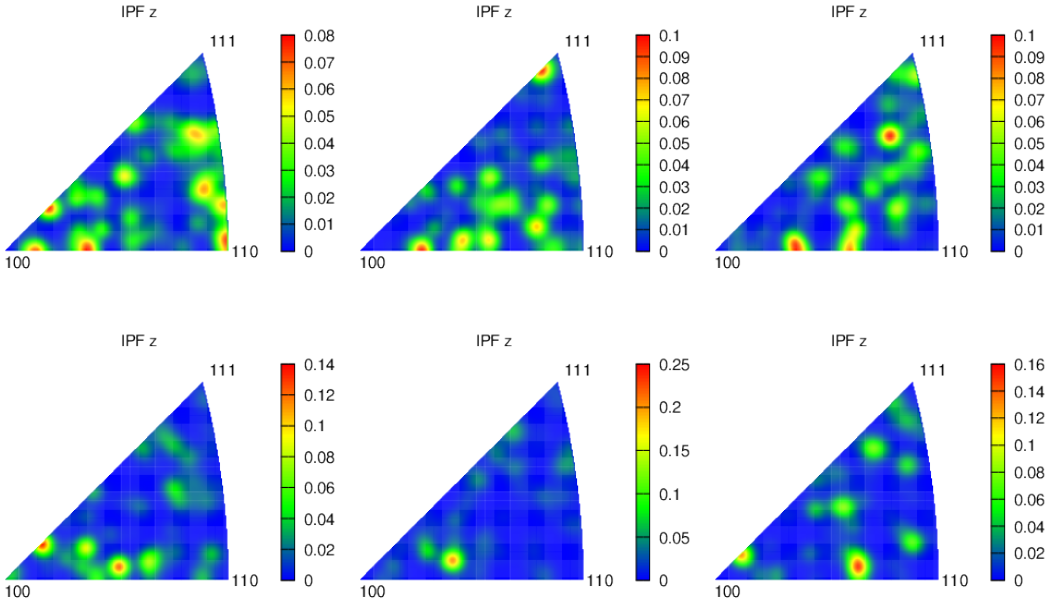

Figure 6: Inverse pole figures (IPF-z) of the grain microstructure for three walls made with different scanning regimes: velocity 600 mm/s and power 195 W (the left ones), velocity 1058 mm/s and power 349 W (the middle ones) and velocity 1600 mm/s and power 500 W (the right ones). Section x = 1.6 mm is on the top and x = 3.2 mm is on the bottom.

produced under high-speed conditions. In Fig. 7 (right panel) the isotherms are almost horizontal and symmetric with respect to the vertical axes, but in the right figure (corresponding to higher velocity) the isotherms are not symmetric due to the presence of solidified regions on the sides of the wall.

It is also possible to perform a statistical analysis of the grain size distribution to determine whether the average grain size depends on the laser scanning regime (Fig. 7). The characteristic grain size was estimated as follows $r = V^{1/3}$, where V is the volume of a grain. The average grain size is approximately 30 μm in all cases, and a slight increase is observed with increasing scanning speed. In particular, higher scanning speeds result in a greater number of grains with sizes in the 40–60 μm range, while the number of grains in the 20–35 μm range decreases.

5 CONCLUSIONS

This work provides for the first time a comprehensive multilayer mesoscale simulation that captures coupled melt pool dynamics and grain growth, offering insights to support process optimization in metal additive manufacturing.

Based on the simulations reported, we can draw the following conclusions. A change in the scanning strategy (layer scanning order) from unidirectional to zigzag can modify and improve the wall morphology, making it more uniform in height and reducing the number of lack-of-fusion regions, but has little effect on the microstructure. On the other hand, the laser speed and power have a much stronger impact on grain structure and wall shape. An increase in the length of the melt pool leads to a disordered grain growth direction. With higher laser speed, the melt pool becomes fractured, and droplets are ejected to the sides of the track. The growth of grains from the sides has a significant impact on the microstructure of the wall.

These insights were made possible by the use of computer simulations. We fine-tuned the process parameters to adjust for the desirable shape of the melt pool. In the simulation of grain growth

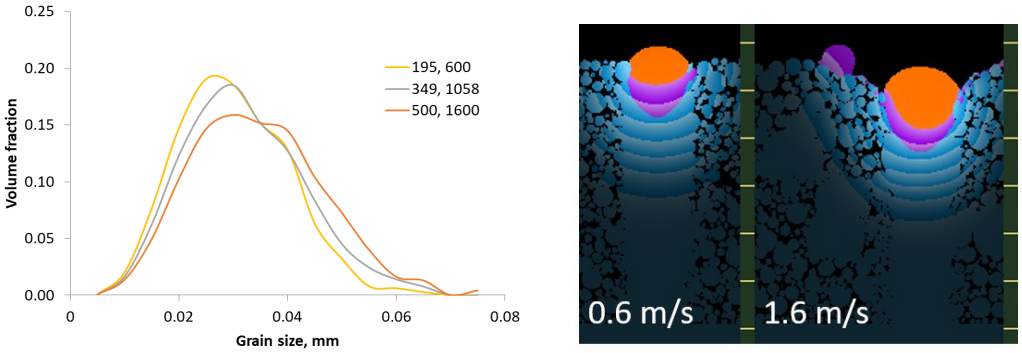

Figure 7: Left: Distribution of grains by size in the representative volume 3x0.1x0.3 mm. Right: Transversal cross-sections of the melt pool. Blue lines indicate isotherms in the solid region, purple lines indicate isotherm in the material, which was solidified during deposition of the upper layer, and orange color indicates liquid region. Upper and lower figures are the sections in different locations.

formation, we obtained the full 3D information for the grains and extracted different statistics. With it, it became possible to analyze the connection of droplet ejection with the grain growth direction.

REFERENCES

[1] B. Brown, W. Everhart, and J. Dinardo, *Rapid Prototyping Journal*, vol. 22, no. 5, pp. 801–809, 2016.

[2] D. Nalum and J. Timhagen, "Study of wall thickness and its impact on microstructure on 316l manufactured with direct metal laser sintering," bachelor thesis, Chalmers University of Technology, 2017.

[3] A. Gaikwad et al., *Smart and Sustainable Manufacturing Systems*, vol. 3, no. 1, pp. 98–121, 2019.

[4] A. Chakraborty et al., *Journal of Materials Science & Technology*, vol. 98, pp. 233–243, 2022.

[5] O. Gokcekaya, et al., *Acta Materialia*, vol. 212, p. 116876, 2021.

[6] Y. Liu and J. Shi, *Advanced Engineering Materials*, vol. 25, no. 14, p. 2201917, 2023.

[7] E. Chauvet et al., *World PM2016 – AM – Powder Bed Based Technologies*, p. 1, 11 2016.

[8] H. Yang et al., *Materials & Design*, vol. 156, pp. 407–418, 2018.

[9] W. E. King et al., *Applied Physics Reviews*, vol. 2, no. 4, 2015.

[10] S. A. Khairallah et al., *Acta Materialia*, vol. 108, pp. 36–45, 2016.

[11] M. Bayat et al., *Additive Manufacturing*, vol. 47, p. 102278, 2021.

[12] Y. Lee and W. Zhang, in *2015 International Solid Freeform Fabrication Symposium*, University of Texas at Austin, 2015.

[13] "KiSSAM simulation software for additive manufacturing." www.kissam.cloud, 2025.

[14] A. Zakirov et al., *Progress in Additive Manufacturing*, pp. 1–18, 2024.

[15] M. Bogdanova et al., *Journal of Manufacturing and Materials Processing*, vol. 8, no. 1, 2024.

[16] A. Zakirov et al., *Additive Manufacturing*, vol. 35, p. 101236, 2020.

[17] D. S. Nakapkin et al., in *Sim-AM 2019: II International Conference on Simulation for Additive Manufacturing*, pp. 297–308, CIMNE, 2019.

[18] B. Korneev et al., *Additive Manufacturing*, vol. 74, p. 103705, 2023.

[19] Z. Gan, K. K. Jones, Y. Lu, and W. K. Liu, *Integrating Materials and Manufacturing Innovation*, vol. 10, no. 2, pp. 177–195, 2021.

[20] S. Wormald et al., *Integrating Materials and Manufacturing Innovation*, vol. 10, no. 3, pp. 348–359, 2021.

[21] Y. Li, Y. Lu, A. A. Amin, and W. K. Liu, *arXiv preprint arXiv:2208.02907*, 2022.

[22] H. Lu, X. Hu, J. Pan, Z. An, and Y. Gu, *The International Journal of Advanced Manufacturing Technology*, vol. 132, no. 11, pp. 5929–5943, 2024.

[23] Z. An, J. Pan, X. Hu, and H. Yang, *International Journal of Heat and Mass Transfer*, vol. 238, p. 126452, 2025.

[24] F. Schmeiser *et al.*, *Journal of Materials Science*, vol. 57, pp. 9663–9677, 2022.

[25] X. Lu, M. V. Li, and H. Yang, *The International Journal of Advanced Manufacturing Technology*, vol. 115, no. 11, pp. 3773–3790, 2021.

[26] X. Lu, X. Yang, X. Zhao, H. Yang, and M. V. Li, *Materials Science and Engineering: A*, vol. 835, p. 142652, 2022.

[27] E. J. Schwalbach, M. G. Chapman, and M. A. Groeber, *Integrating Materials and Manufacturing Innovation*, vol. 10, no. 3, pp. 319–337, 2021.

[28] R. Wrobel et al., *Materials & Design*, vol. 238, p. 112652, 2024.

[29] A. Bhatt et al., *Additive Manufacturing*, vol. 77, p. 103809, 2023.

[30] W. A. Morais and F. J. G. Landgraf, *Tecnol Metal Mater Min.*, vol. 20, 2023.

[31] M. Bayat et al, *Progress in Materials Science*, vol. 138, p. 101129, 2023.

[32] E. Attar and C. Körner, *International Journal of Heat and Fluid Flow*, vol. 32, no. 1, pp. 156–163, 2011.

[33] T. Krüger et al., "The lattice Boltzmann method," *Springer International Publishing*, vol. 10, no. 978-3, pp. 4–15, 2017.

[34] M. Thies, *Lattice Boltzmann modeling with free surfaces applied to in-situ gas generated foam formation*. Ph.d. thesis, University of Erlangen-Nuremberg, Erlangen, 2005.

[35] N. Govender, D. N. Wilke, and S. Kok, *SoftwareX*, vol. 5, pp. 62–66, 2016.

[36] M. Rappaz and C.-A. Gandin, *Acta metallurgica et materialia*, vol. 41, no. 2, pp. 345–360, 1993.

[37] Y. Zhi et al., *Materials*, vol. 17, no. 6, p. 1370, 2024.

[38] C.-A. Gandin and M. Rappaz, *Acta Materialia*, vol. 45, no. 5, pp. 2187–2195, 1997.

[39] C.-A. Gandin and M. Rappaz, *Acta metallurgica et materialia*, vol. 42, no. 7, pp. 2233–2246, 1994.

[40] Y. Yu, Y. Li, F. Lin, and W. Yan, *Additive Manufacturing*, vol. 47, p. 102284, 2021.

[41] Y. Zhang and J. Zhang, *Additive Manufacturing*, vol. 28, pp. 750–765, 2019.

[42] Y. Lian, S. Lin et al., *Computational Mechanics*, vol. 61, pp. 543–558, 2018.

[43] A. Zakirov et al, *Additive Manufacturing*, vol. 35, p. 101236, 2020.

[44] A. S. Sabau et al, *Metallurgical and Materials Transactions B*, vol. 51, pp. 1263–1281, 2020.

[45] S. Ghosh et al, *JOM*, vol. 70, no. 6, 2018.

[46] J. S. Weaver, J. C. Heigel, and B. M. Lane, *Journal of Manufacturing Processes*, vol. 73, pp. 26–39, 2022.

[47] "Air Force Research Laboratory (AFRL) Additive Manufacturing (AM) Modeling Challenge Series," 2020.

[48] X. Zhang et al, *Journal of Laser Applications*, vol. 31, no. 3, 2019.

[49] T. M. Rodgers et al, *Computational Materials Science*, vol. 135, pp. 78–89, 2017.